frontiers | Frontiers in Mechanical Engineering

TYPE Original Research
PUBLISHED 08 January 2026
DOI 10.3389/fmech.2025.1658430

OPEN ACCESS

EDITED BY
Nima Rezazadeh,
Università della Campania Luigi Vanvitelli, Italy

REVIEWED BY
Joshuva Arockia Dhanraj,
Dayananda Sagar University, India
Panpan Xu,
The University of Sheffield, United Kingdom

*CORRESPONDENCE
Shirsendu Sikdar,
✉ s.sikdar@hud.ac.uk

RECEIVED 02 July 2025
REVISED 01 December 2025
ACCEPTED 15 December 2025
PUBLISHED 08 January 2026

CITATION
Pillai AJ and Sikdar S (2026) Guided wave based health monitoring of composite wind turbine blades: multi-level damage assessment. *Front. Mech. Eng.* 11:1658430. doi: 10.3389/fmech.2025.1658430

Guided wave based health monitoring of composite wind turbine blades: multi-level damage assessment

Anjaly J. Pillai[1,2] and Shirsendu Sikdar[3]*

[1]Institute of Fluid-Flow Machinery, Polish Academy of Sciences, Gdansk, Poland, [2]Department of Civil Engineering, Amrita School of Engineering, Coimbatore, India, [3]School of Computing and Engineering, University of Huddersfield, Huddersfield, United Kingdom

Structural health monitoring (SHM) of wind turbines is critical for maintaining continuous operation, minimizing maintenance expenses, and maximizing energy production. Recent advancements in sensor technology have made it possible to gather extensive ultrasonic guided wave (UGW) data from wind turbine components, enabling assessment of their structural integrity. This research examines UGW-based nondestructive evaluation techniques applied to composite wind turbine blades under varied structural conditions using experimental and numerical analysis. UGW signals recorded through an actuator-sensor network contain essential information on blade health. A Random Forest model is used to predict changes in A0 and S0 mode group velocities and amplitudes due to erosion/corrosion, longitudinal debonding, and transverse debonding across damage sizes ranging from 0 to 40 mm. To assess prediction reliability, 95% confidence intervals are included as uncertainty bands; narrower bands suggest higher confidence, while a wider band indicates greater uncertainty. Sensitivity analysis highlights the impact of damage size and type on UGW signal properties, supporting improved predictions. This study underscores the potential of UGW-based SHM to enhance wind turbine reliability and promote sustainable energy generation.

KEYWORDS

composite wind turbine blade, damage detection, structural health monitoring, ultrasonic guided waves, uncertainty quantification

1 Introduction

Wind energy is a form of renewable energy that has gained significant importance in recent decades. Many countries are starting to invest in the wind energy sector. The use of this form of energy is not expected to decrease over time (Márquez et al., 2012; Maas, 2023). The growing trend in this sector is the manufacture and deployment of bigger wind turbines. Akhtar et al. (2024) studied the wakes from wind farms with small and large wind turbines in the North Sea. The work analysed the effect of these turbines on near-surface climate and power production. The findings showed that wind farms with larger turbines have a smaller impact on the near-surface climate compared to farms with many small turbines. This implies that large wind turbines may have less effect on ocean dynamics and the ecosystem. These turbines are designed to work in harsh climates and in areas that are hard to reach (Grindheim et al., 2023). As a result, structural health monitoring (SHM) becomes essential. It allows for remote assessment of structural integrity, reduces periodic inspection costs, minimizes downtime and breakdowns, and helps prevent unnecessary component replacements during service (Schulz and Sundaresan, 2006).

The critical component susceptible to damage in wind turbines is the wind turbine blade (WTB). The WTBs are constructed in conjunction with other parts of the turbine. These form the primary component in capturing wind energy, making them susceptible to environmental forces. The efficiency and functionality of turbines are compromised when WTBs are damaged. Also, the value of a WTB is approximately 15%–20% of the total cost of the wind turbine (Li et al., 2014). Therefore, it becomes essential to study the importance of operation and mitigation strategies to reduce WTB damage (Dimitrova et al., 2022; Algolfat et al., 2023; Dadashbaki et al., 2025).

WTBs are made from composites such as glass fibre, carbon fibre, balsa wood, or foam. These materials are chosen to improve efficiency by increasing the strength-to-weight ratio. However, their composite structures are prone to damage such as disbond or delamination due to manufacturing defects, ageing, or repeated impacts. Blades can also corrode when exposed to harsh environments (Raju et al., 2024). The repetition of loads causes fatigue damage to build up, which leads to material cracks even early in their service life (Gaidai et al., 2023). Studies on detecting and mitigating internal damage have been carried out to prevent structural failure (Giurgiutiu et al., 2002; Giurgiutiu, 2005; Sikdar et al., 2024).

Many studies have examined health monitoring techniques for detecting damage in WTBs. These techniques include visual inspection, acoustic emission, ultrasonic testing (UT), static strain measurements, and short-range Doppler radar (Joosse et al., 2002; Verijenko and Verijenko, 2005; Yan et al., 2007; Schubel et al., 2013; Zhang and Jackman, 2014; Habibi et al., 2015; Skaga, 2017; Zhao et al., 2021; Bejger et al., 2023). Ultrasonic guided wave testing is often used because of its wide range of transducers, high defect sensitivity, and ability to detect damage over long distances (Nam et al., 2018; Shoja et al., 2018).

Claytor et al. (2010) tested a multi-scale SHM system for WTBs using piezoelectric transducer (PZT) active sensing. The study detected damage on a CX-100 blade section by integrating Lamb wave propagation, frequency response analysis, and time-series (ARX model) techniques. Lamb waves provided good damage localisation but needed high power. Frequency response analysis proved reliable and moderately efficient. The time-series ARX model was best for detecting subtle changes, but required more computing. Taylor et al. (2012) conducted a full-scale fatigue test of a 9 m CX-100 WTB to evaluate SHM techniques under realistic damage progression. The blade was instrumented with piezoelectric (guided-wave), diffuse wave-field, frequency response sensors, and an experimental wireless low-power SHM platform. It was observed from the study that guided-wave sensing was best for local and early damage detection.

Further, trailing edge damage of a WTB is experimentally detected using the aerofoil aerodynamic noise measurement (Zhang et al., 2022). The experimental investigation includes the effect of varying mean flow velocities, inflow turbulence intensities and angles of attack for the detection of trailing edge damage. It was observed that the damage detection was possible by understanding the tonal noise features. Ou et al. (2021) set up an experimental benchmark for SHM using a small-scale WTB considering temperature variations. The study shows that environmental conditions (especially temperature) have a measurable effect on the vibration response of the blade. Xue et al. (2023) developed Multi-task Complex Hierarchical Sparse Bayesian Learning, which encodes multi-task learning using guided wave data at multiple frequencies to ensure consistency in damage location across tasks. This algorithm outperforms single-task models in terms of the localisation accuracy for multiple damage locations. Gómez Muñoz et al. (2019) developed an approach for disunity detection between layers of composite WTBs. The method was able to detect the presence of disbonds in the damaged blade. It was also concluded from the study that despite the large attenuation in composite materials, UGWs were able to assess the condition of the blade. A case study on the use of condition monitoring for detecting damage on a real WTB using non-linear acoustics and guided waves was done by Yang et al. (2018). It was observed from the study that detection using non-linear acoustics was insensitive to damage. In comparison to this method, the guided wave pitch-catch approach was accurate in detecting damage. Sinner et al. (2023) investigated the sensitivity of a preview-enabled model predictive controller for wind turbines. This was developed using upstream wind speed measurements. This improved the rotor speed regulation and was robust to timing errors in wind delay estimation.

An approach to identify delamination in laminated composites was proposed using Lamb wave propagation (Su et al., 2002). The noise was suppressed using a Wavelet transform-based signal processing technique. The detection of damage was found to be accurate using this method. Hay et al. (2003) developed a damage localisation algorithm for non-destructive evaluation of core crush damage in honeycomb composite sandwich panels using ultrasonic guided waves. The developed algorithm enabled accurate mapping of damage within the sensor network. Lanza Discalea et al. (2007) monitored a composite wing skin-to-spar joint in an unmanned aerial vehicle using UGWs. Poorly curved adhesives and disbanded interfaces were simulated. Using a semi-analytical finite element (FE) method considering viscoelastic damping, dispersion wave propagation was obtained. This was verified using experimental tests. It was observed from the work that across the defective bonds, there is an increase in the ultrasonic strength of transmission.

Oliveira et al. (2020) proposed a method to identify structural damage in WTBs using ultrasonic non-destructive testing (NDT) combined with novelty detection. The process is to obtain ultrasonic signals from the blade in its healthy state, preprocess (wavelet denoising and principal component analysis (PCA)), and then apply a novelty detector trained only on healthy data so that deviations indicate damage. The study covers signals recorded from WTBs under controlled conditions; the focus is on detecting any damage rather than specifically localising it. The novelty detection approach was effective in distinguishing damaged from undamaged states in the tested blades, despite not having explicit damage-type training data. Mendikute et al. (2025) and Zhu et al. (2025) presented a deep learning–based approach for detecting internal defects in wind turbine blades using UT data. Convolution Neural Networks (CNNs) were applied to automatically learn and classify patterns from ultrasonic scans.

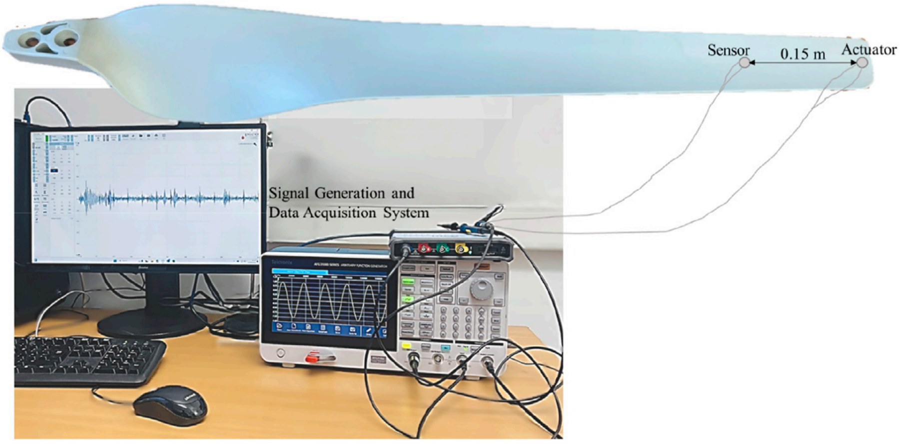

FIGURE 1
Experimental setup for guided wave-based inspection of WTB samples.

This approach achieved high accuracy in defect detection, outperforming conventional feature-based UT analysis. Chai et al. (2025) developed an SHM system for WTBs using UGW technology. Failure modes like gelcoat cracks and adhesive joint debonding were detected using UGW across multiple frequency bands.

The existing research established that the ultrasonic guided wave method is efficient in localising and characterising the defects in layered composite materials (Lowe et al., 2000; Camanho, 2002). The advantage of this technique is that the wave structure is dependent on the frequency and phase velocity, and it can also propagate long distances with penetration in hidden layers (Humer et al., 2022; Junqueira et al., 2024). Although work has been done to detect damage using guided waves in WTBs, wave attenuation occurs in the usage of guided waves, thus limiting the application to small regions. Additionally, the complex design of WTBs hinders the application of this technique commercially, as the process of extracting information from the complex signals becomes difficult. Thus, the need for effective monitoring solutions for WTBs becomes more critical.

This paper examines guided wave propagation in composite WTBs affected by common damage types. UGWs are well-suited for this task due to their ability to propagate over long distances, allowing early-stage damage detection with minimal sensor deployment. This study establishes baseline guided wave responses from healthy WTBs, which are compared against damaged cases using three-dimensional finite element modeling in ABAQUS. Numerical results are validated experimentally, and parametric analyses assess the impact of various damage types and severities on wave behavior. Analytical and machine learning techniques are then applied to evaluate prediction accuracy and reliability. By integrating experimental, numerical, and machine learning approaches, the framework enhances damage detection precision, reduces extensive testing requirements, and improves scalability and robustness beyond prior single-method studies. Future work will focus on autonomous damage detection and characterization using data-driven models.

2 Experimental analysis

Laboratory experiments have been carried out on multiple composite WTB samples using a pair of PZT transducers (8 mm dia., 0.5 mm thin) serve as Actuator and/or Sensor mounted to the blade surface for actuation and reception of guided wave signals. A signal generator and data acquisition system are used to operate the PZTs. The PZT disc sensors were designed primarily for longitudinal wave excitation and reception, optimized for the S0 and A0 Lamb wave modes.

The experimental setup with a healthy blade sample is shown in Figure 1. These blades are made of a 3 mm thick glass fibre reinforced composite (GFRC) laminate (0°/90°/45°/-45°/90°/0°). In the study, four types of WTB samples are considered- (i) healthy WTB, (ii) WTB with edge erosion/corrosion (25 mm long), (iii) WTB with longitudinal debond (35 mm × 6.5 mm) and (iv) WTB with transverse debond (45 mm × 6.5 mm): H, D1, D2, and D3 respectively.

These debonds were artificially introduced to the blade samples. The disbond locations in the WTBs are schematically represented in Figure 2. In the experiments, 5-cycle sine burst signals of 150 kHz are applied as the PZT excitation signal for all experimental analyses to confine the frequency content narrowly and reduce unwanted reflections. During data acquisition, signals were averaged multiple times to enhance stability and suppress random electrical and environmental noise, particularly at low frequencies (<4 kHz). Raw signals were digitized using a high-resolution data acquisition system and subsequently processed through bandpass filtering and time-windowing to isolate the guided wave packets.

To ensure repeatability and consistency, each experimental test was performed multiple times under identical conditions, and the sensor signals were recorded for each trial. Statistical analysis of the repeated measurements showed minimal variation in both signal amplitude and time-of-flight, confirming high consistency. Furthermore, the experimental setup-including sensor placement, excitation parameters, and environmental conditions-was carefully controlled to reduce variability. These measures collectively ensured that the experimental results were reliable and reproducible.

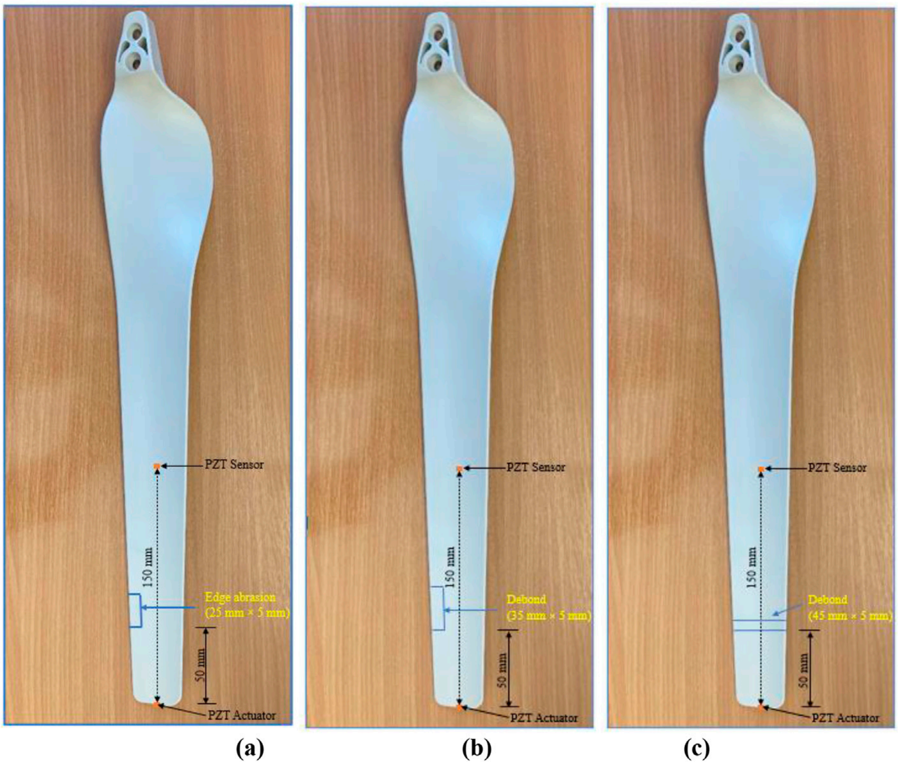

FIGURE 2
Schema of WTBs for **(a)** edge erosion/corrosion, **(b)** longitudinal and **(c)** transverse debond.

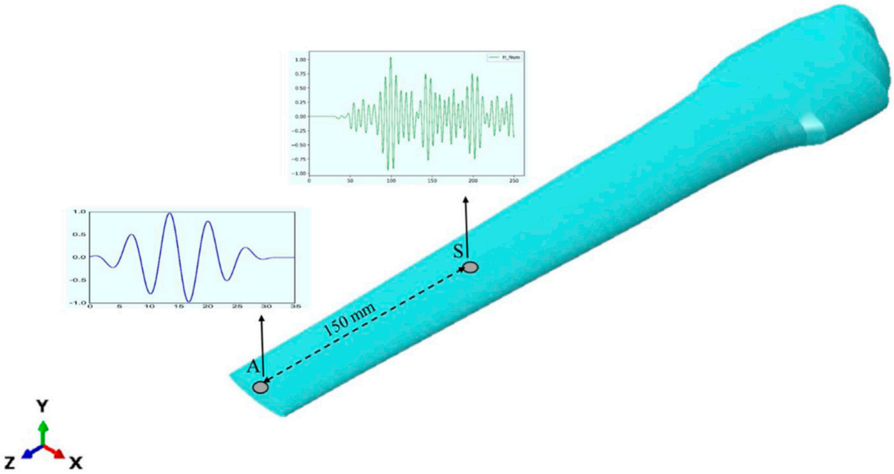

FIGURE 3
WTB model in ABAQUS for simulation of guided waves under variable conditions. (A is the actuation location and S is the sensing location).

3 Numerical modelling of wind turbine blade

The prediction of intricate interactions between elastic wave dynamics and damage in multi-layered composite WTBs is challenging due to complex structural geometry and boundary conditions. This becomes more difficult for damage types such as cracks, corrosion and debonding. Therefore, a numerical analysis using FE simulations has been done using ABAQUS software to investigate the influence of the damage types on the propagation of guided waves in composite blades.

This is achieved using a 3D numerical modelling of the composite WTB and simulating guided wave propagation within the blade. This simulation closely mirrors laboratory experiments

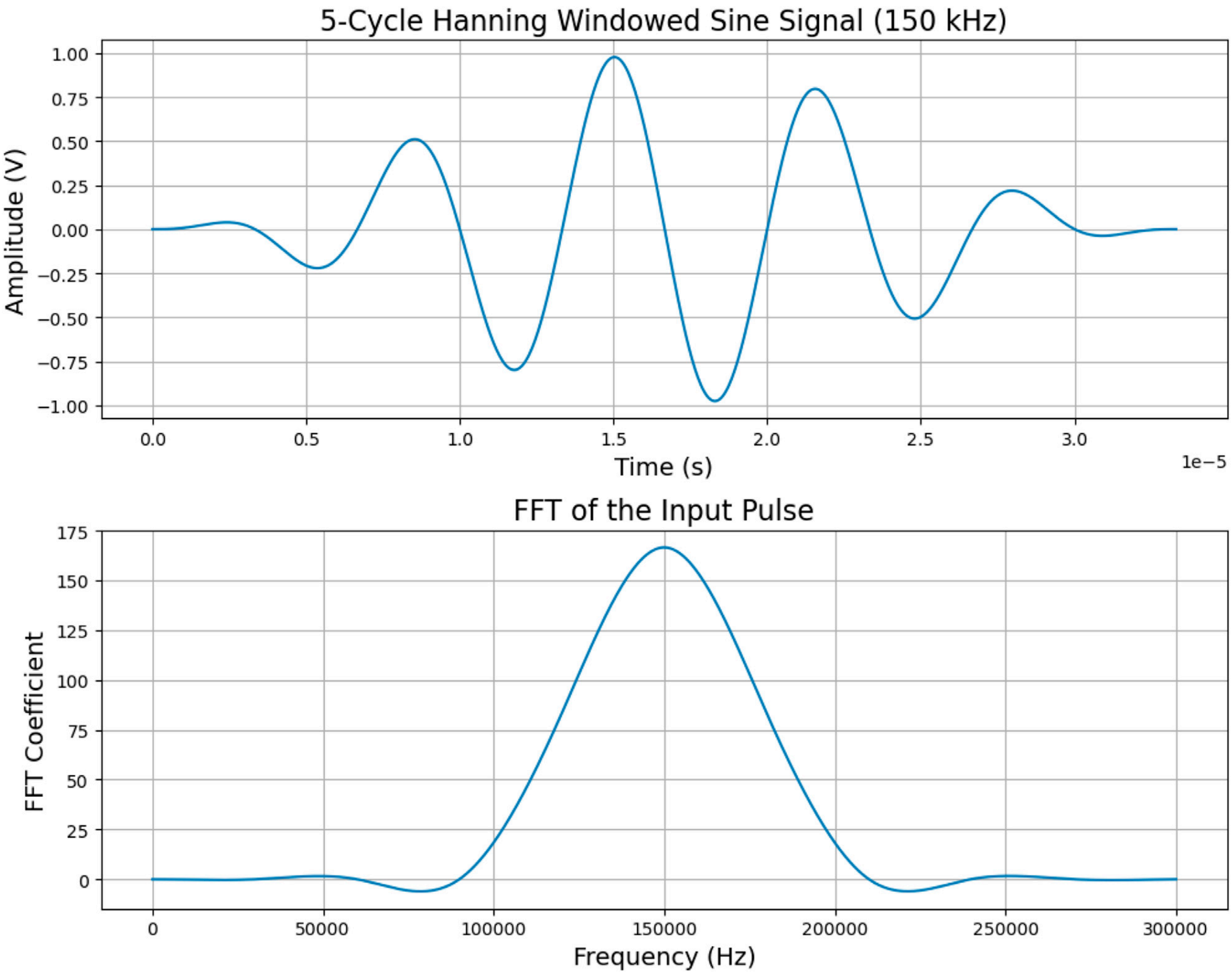

FIGURE 4
Actuation signal in time domain (top) and its frequency response from Fast Fourier Transform (FFT) (bottom).

employing a surface-mounted actuator and sensor system as represented in Figure 3. These numerical simulations of the actuator-induced guided wave propagation within the glass-fibre composite blade prove to be intriguing and demanding. The FE modelling and analysis of the WTB with dimensions used in a real-world scenario was computationally expensive, considering the number of elements and computational time. So, a scaled-down model of the WTB is used. The dimensions of the WTB used in FE analysis are similar to the dimensions used in the experimental study. Thus, a 500 mm long WTB was modelled in ABAQUS/CAE 2022 version 6.22.

Four types of FE models are developed, namely (i) healthy WTB, (ii) WTB with edge erosion/corrosion, (iii) WTB with longitudinal debond and (iv) WTB with transverse debond; represented as H, D_1, D_2 and $D_{3,}$ respectively. In the FE simulation, guided waves are actuated from the actuation location, 'A' and the guided waves (time domain) are recorded at the sensing position, 'S', illustrated in Figure 3. The actuation signals are selected as a 5-cycle sine burst 150 kHz signal, which is shown in Figure 4 (top), and the frequency response of the actuation signal is shown in Figure 4 (bottom). Table 1 outlines the homogenised material properties used in the FE analysis of composite WTBs (Barr and Jaworski, 2019).

In Table 1, E_{11}, E_{22} and E_{33} represent the longitudinal modulus of elasticity, modulus of elasticity in the transverse direction and modulus of elasticity along the thickness respectively. G_{12}, G_{23} and G_{13} refer to the modulus of rigidities in 1–2 plane, 2–3 plane and 1–3 plane respectively. ν_{12}, ν_{13}, ν_{23} are the Poisson's ratios in 1–2 plane, 1–3 plane and 2–3 plane, respectively; and ρ is the density of material.

Damage in composite materials occurs in two stages, namely damage initiation and evolution. Damage initiation refers to the onset of degradation in a composite material (Kalgutkar and Banerjee, 2024; Sikdar and Banerjee, 2016). The failure modes linked to Hashin's criteria are fibre and matrix failure modes. These implicate four different modes of damage initiation, which are fibre tension, fibre compression, matrix tension and matrix compression. The following Equations 1–4 are considered for the initiation criteria (Hashin, 1980):

Fibre tension ($\hat{\sigma}_{11} \geq 0$)

TABLE 1 Elastic material properties of the WTB (Barr and Jaworski, 2019).

Material	E_{11} (GPa)	E_{22} (GPa)	E_{33} (GPa)	G_{12} (GPa)	G_{13} (GPa)	G_{23} (GPa)	ν_{12} (GPa)	ν_{13} (GPa)	ν_{23} (GPa)	ρ (kg/m³)
GFRC	41	9	9	4.1	4.1	4.1	0.27	0.27	0.27	1890

$$F_f^t = \left(\frac{\hat{\sigma}_{11}}{X^T}\right)^2 + \alpha\left(\frac{\hat{\tau}_{12}}{S^L}\right)^2 \tag{1}$$

Fibre compression $(\hat{\sigma}_{11} < 0)$

$$F_f^c = \left(\frac{\hat{\sigma}_{11}}{X^C}\right)^2 \tag{2}$$

Matrix tension $(\hat{\sigma}_{22} \geq 0)$

$$F_m^t = \left(\frac{\hat{\sigma}_{22}}{Y^T}\right)^2 + \alpha\left(\frac{\hat{\tau}_{12}}{S^L}\right)^2 \tag{3}$$

Matrix compression $(\hat{\sigma}_{22} < 0)$

$$F_m^c = \left(\frac{\hat{\sigma}_{22}}{2S^T}\right)^2 + \left[\left(\frac{Y^C}{2S^T}\right)^2 - 1\right]\frac{\hat{\sigma}_{22}}{Y^C} + \left(\frac{\hat{\tau}_{12}}{S^L}\right)^2 \tag{4}$$

where, X^T, X^C, Y^T, Y^C, S^L, S^T and α denotes tensile strength in the direction of fibre, compressive strength in the direction of fibre, tensile strength in the direction perpendicular to the fibre direction, compressive strength in the direction perpendicular to the fibre direction, longitudinal shear strength, transverse shear strength and coefficient that determines the contribution of the shear stress to the fibre tensile initiation criterion respectively. $\hat{\sigma}_{11}$, $\hat{\sigma}_{22}$, $\hat{\tau}_{12}$ denote the components of effective stress tensor, $\hat{\sigma}$; which is computed using the following equation

$$\hat{\sigma} = M\sigma \tag{5}$$

where, σ and M are the nominal stress and damage operator respectively. The damage operator in Equation 5 is given as

$$M = \begin{bmatrix} \frac{1}{1-d_f} & 0 & 0 \\ 0 & \frac{1}{1-d_m} & 0 \\ 0 & 0 & \frac{1}{1-d_s} \end{bmatrix} \tag{6}$$

In Equation 6, d_f, d_m and d_s represent the internal damage variables characterising fibre matrix and shear damage respectively. These variables are derived from the damage variables d_f^t, d_f^c, d_m^t, d_m^c corresponding to the fibre tension, fibre compression, matrix tension and matrix compression modes respectively. These modes in terms of the damage variables are given below

$$d_f = \begin{cases} d_f^t \; if \; \hat{\sigma}_{11} \geq 0 \\ d_f^c \; if \; \hat{\sigma}_{11} < 0 \end{cases} \tag{7}$$

$$d_m = \begin{cases} d_m^t \; if \; \hat{\sigma}_{22} \geq 0 \\ d_m^c \; if \; \hat{\sigma}_{22} < 0 \end{cases} \tag{8}$$

$$d_s = 1 - \left(1 - d_f^t\right)\left(1 - d_f^c\right)\left(1 - d_m^t\right)\left(1 - d_m^c\right) \tag{9}$$

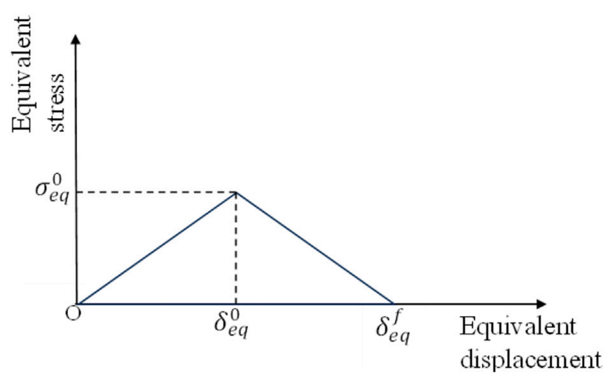

FIGURE 5
Graphical representation of equivalent stress and equivalent displacement.

It is to be noted that prior to any damage initiation and evolution the damage operator, M, is equal to the identity matrix, i.e., $\hat{\sigma} = \sigma$. Once damage initiation and evolution have occurred for at least one mode, the damage operator becomes significant in the criteria for damage initiation of other modes. The effective stress, $\hat{\sigma}$, is intended to represent the stress acting over the damaged area that effectively resists the internal forces. The Hashin's damage initiation criteria integrated on ABAQUS follows the damage initiation as explained above (Hashin and Rotem, 1973; Lapczyk and Hurtado, 2007).

Damage evolution represents the rate of degradation of material stiffness once the damage initiation criteria has been reached. The response of the material with damage initiation and evolution is computed using the following Equation 10 (Matzenmiller et al., 1995)

$$\sigma = C_d \varepsilon \tag{10}$$

where, ε is the strain and C_d is the damage elasticity matrix (Matzenmiller et al., 1995), which is expressed as

$$C_d = \frac{1}{D}\begin{bmatrix} \left(1-d_f\right)E_1 & \left(1-d_f\right)(1-d_m)\nu_{21}E_1 & 0 \\ \left(1-d_f\right)(1-d_m)\nu_{12}E_2 & (1-d_m)E_2 & 0 \\ 0 & 0 & (1-d_s)GD \end{bmatrix} \tag{11}$$

$$D = 1 - \left(1-d_f\right)(1-d_m)\nu_{12}\nu_{21} \tag{12}$$

In Equations 11 and 12, d_f, d_m and d_s reflects the present state of fibre damage, matrix damage and shear damage. E_1 is the modulus of elasticity in the direction of fibres, E_2 is the modulus of elasticity in the direction perpendicular to the fibres, G is the shear modulus and ν_{12} and ν_{21} are the Poisson's ratios. The damage variables d_f, d_m and d_s are given in Equations 7–9.

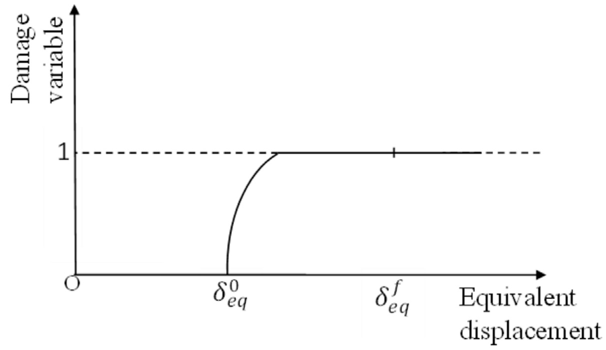

FIGURE 6
Graphical representation of damage variable and equivalent displacement.

The damage variable evolves with reference to the stress displacement behaviour for each of the four different modes as shown in Figure 5 (Matzenmiller et al., 1995; Warren et al., 2016).

In Figure 5, the positive slope of the stress-displacement curve corresponds to the period before damage initiation, and the material properties are linear elastic in nature. The negative slope corresponds initiation of damage, which is achieved by the evolution of the respective damage variables, given in equations below.

Fibre tension $(\hat{\sigma}_{11} \geq 0)$

$$\delta_{eq}^{ft} = L^C\sqrt{\langle\varepsilon_{11}\rangle^2 + \alpha\varepsilon_{12}^2} \tag{13}$$

$$\sigma_{eq}^{ft} = \frac{\langle\sigma_{11}\rangle\langle\varepsilon_{11}\rangle + \alpha\tau_{12}\varepsilon_{12}}{\delta_{eq}^{ft}/L^C} \tag{14}$$

Fibre compression $(\hat{\sigma}_{11} < 0)$

$$\delta_{eq}^{fc} = L^C\langle-\varepsilon_{11}\rangle \tag{15}$$

$$\sigma_{eq}^{fc} = \frac{\langle-\sigma_{11}\rangle\langle-\varepsilon_{11}\rangle}{\delta_{eq}^{fc}/L^C} \tag{16}$$

Matrix tension $(\hat{\sigma}_{22} \geq 0)$

$$\delta_{eq}^{mt} = L^C\sqrt{\langle\varepsilon_{22}\rangle^2 + \varepsilon_{12}^2} \tag{17}$$

$$\sigma_{eq}^{mt} = \frac{\langle\sigma_{22}\rangle\langle\varepsilon_{22}\rangle + \tau_{12}\varepsilon_{12}}{\delta_{eq}^{mt}/L^C} \tag{18}$$

Matrix compression $(\hat{\sigma}_{22} < 0)$

$$\delta_{eq}^{mc} = L^C\sqrt{\langle-\varepsilon_{22}\rangle^2 + \varepsilon_{12}^2} \tag{19}$$

$$\sigma_{eq}^{mc} = \frac{\langle-\sigma_{22}\rangle\langle-\varepsilon_{22}\rangle + \tau_{12}\varepsilon_{12}}{\delta_{eq}^{mc}/L^C} \tag{20}$$

In Equations 13–20, L^C is the characteristic length of elements with a plane stress formulation and the symbol $\langle\,\rangle$ represents the Macauley bracket operator, which is defined for every $\alpha \in \Re$ as $\langle\alpha\rangle = (\alpha + |\alpha|)/2$. After damage initiation, $\delta_{eq} \geq \delta_{eq}^{0}$, the damage variable for a particular mode is given below in Equation 21

$$d = \frac{\delta_{eq}^{f}\left(\delta_{eq} - \delta_{eq}^{0}\right)}{\delta_{eq}\left(\delta_{eq}^{f} - \delta_{eq}^{0}\right)} \tag{21}$$

where δ_{eq}^{0} is the initial equivalent displacement at which the initiation criterion for that mode was met, and δ_{eq}^{f} is the displacement at which the material is completely damaged in this failure mode. The behaviour pertaining after damage initiation (ABAQUS, 2008) is presented in Figure 6.

The values of δ_{eq}^{0} for different modes depend on the elastic stiffness and the strength parameters specified as part of damage initiation. The energy dissipated due to failure; G^C corresponds to each failure mode and is obtained from the area of triangle in the equivalent stress and equivalent displacement plot. The values of δ_{eq}^{f} for different modes depend on the respective G^C values (Matzenmiller et al., 1995; Warren et al., 2016). The materials are assumed to have a linear softening behaviour for the damage evolution process.

3.1 Damage modelling

Hashin's damage criteria is considered for damage initiation, and damage evolution is based on the energy dissipated in each failure mode. The material properties used for damage initiation and evolution for all the damage models are given in Table 2 (Boudounit et al., 2020).

The finite element modelling process is outlined as follows: The wind turbine blade geometry was generated by extruding an elliptical reference cross-section along the blade span. Additional cross-sections were generated using longitudinally positioned datum planes. These profiles were connected via solid extrusion in Abaqus/CAE and then appropriately partitioned to achieve a high-quality mesh. The resulting solid model was partitioned and converted into a shell-based representation to facilitate accurate definition of the composite layup. Material properties and ply orientations were assigned using the Shell Composite Section module, in alignment with the experimental specimen described in Section 2. The mesh consisted of four-node, doubly curved S4R shell elements (element size: 0.5 mm × 0.5 mm), with reduced integration and hourglass control enabled.

The damage modelling employed a combination of Hashin failure criteria and Cohesive Zone Modelling (CZM) concepts to capture the initiation and evolution of erosion, longitudinal debonding, and transverse debonding. Damage was introduced through zero-volume regions at predefined nodes in case of edge erosion, longitudinal debond and transverse debond, where node-to-node connections were selectively removed to represent the local loss of stiffness. For longitudinal and transverse debonding, an equivalent scaling factor of 0.0132 mm was applied to the damaged region, with corresponding modulus and shear values of 850 MPa (ABAQUS, 2017). Erosion damage was simulated using a thickness factor of 1×10^{-6} mm, combined with surface-based traction-separation behaviour. To replicate cohesive effects without explicit cohesive elements, connector damage mechanisms were defined through force-based initiation and tabular motion-based evolution laws (ABAQUS, 2017).

TABLE 2 Material properties of the WTB for damage initiation and evolution.

Material	X^T (GPa)	X^C (GPa)	Y^T (GPa)	Y^C (GPa)	S^L (GPa)	S^T (GPa)	G_{ft}^C (N/m)	G_{fc}^C (N/m)	G_{mt}^C (N/m)	G_{mc}^C (N/m)
GFRC	1.0123	0.978	0.0295	0.1718	0.0353	0.0353	300	300	600	600

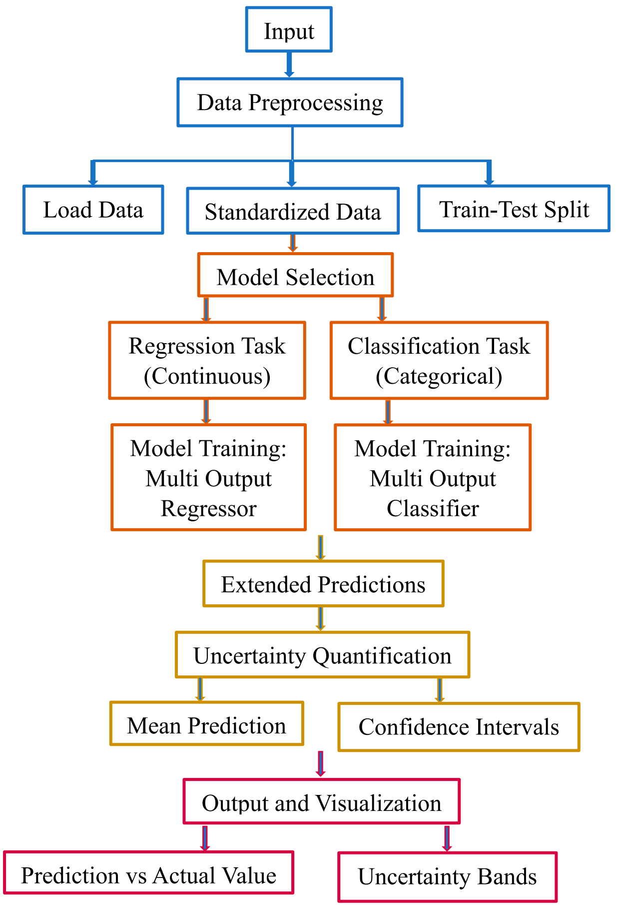

FIGURE 7
Flowchart of the UQ and prediction model.

To enable direct comparison with experimental results, the boundary conditions and loading scenarios in the finite element analysis were made fully consistent with those used in the experimental tests. The blade root was modelled as fully constrained, accurately representing the clamping mechanism employed in the test setup. A 5-cycle sine-Hanning excitation pulse at 150 kHz, identical to the one detailed in Section 2, was applied at the actuator location to initiate guided wave propagation. Simulations were conducted once for the undamaged (healthy) condition and three times for each damage scenario. The analysis was run using Dynamic Explicit in ABAQUS CAE 2022 version 6.22. The time step considered is 1×10^{-7} s, and the total time considered for analysis is 0.005 s. The CPU time required to run the healthy WTB model was 1.042 h; the analysis was run on one core, implying that parallelisation was minimal.

4 Uncertainty quantification (UQ) and prediction

This section presents the relationship between different types of damage sizes and variations in group velocity or amplitudes. The goal is to assess the model's accuracy within known data and its reliability in extrapolating beyond observed values. In this Random Forest model, each tree generates an individual prediction, and the overall prediction is the mean of all trees in the ensemble. Uncertainty is quantified by calculating the standard deviation of predictions from each tree, capturing the variability in the model's outputs. The confidence interval (C_{int}), visualized as shaded uncertainty bands, is calculated in Equation 22 as:

$$C_{int} = \hat{Y} \pm 1.96 \times \sigma \tag{22}$$

where $\hat{Y}$ is the predicted mean and σ is the standard deviation, providing a 95% confidence interval under a normality assumption. Figure 7 flowchart explains the prediction model.

The uncertainty bands visualize the confidence in the predictions: narrower bands indicate higher certainty, while wider bands suggest greater variability and lower confidence. This approach allows robust assessment of model performance on both observed and extrapolated damage cases and guides future data collection to improve prediction accuracy.

Implemented in Python, the Random Forest model predicts changes in guided wave mode group velocities and amplitudes caused by damage types such as erosion, corrosion, and debonding in composite wind turbine blades, while simultaneously estimating prediction uncertainty.

Key time- and frequency-domain features extracted from the ultrasonic guided wave signals include peak amplitude, time of flight, energy content, entropy, skewness, kurtosis, and spectral centroid. These features were selected due to their established sensitivity to damage-induced changes in wave propagation. To enhance model efficiency and accuracy, a correlation-based feature selection method was applied to remove redundant features, retaining only those strongly correlated with damage size and type (such as peak amplitude, RMS amplitude, group velocity, and first-arrival time of the primary wave modes and the frequency-domain features like dominant frequency shift, spectral centroid and bandwidth).

The Random Forest model's predictive accuracy was evaluated using the Root Mean Square Error (RMSE), which measures the average magnitude of errors between predicted and actual damage measurements. RMSE is particularly useful because it penalizes larger errors more heavily, providing a reliable measure of model precision. Lower RMSE values reflect more accurate predictions and closer alignment with true damage values. The reported RMSE demonstrates the model's effectiveness in estimating damage parameters in composite wind turbine blades.

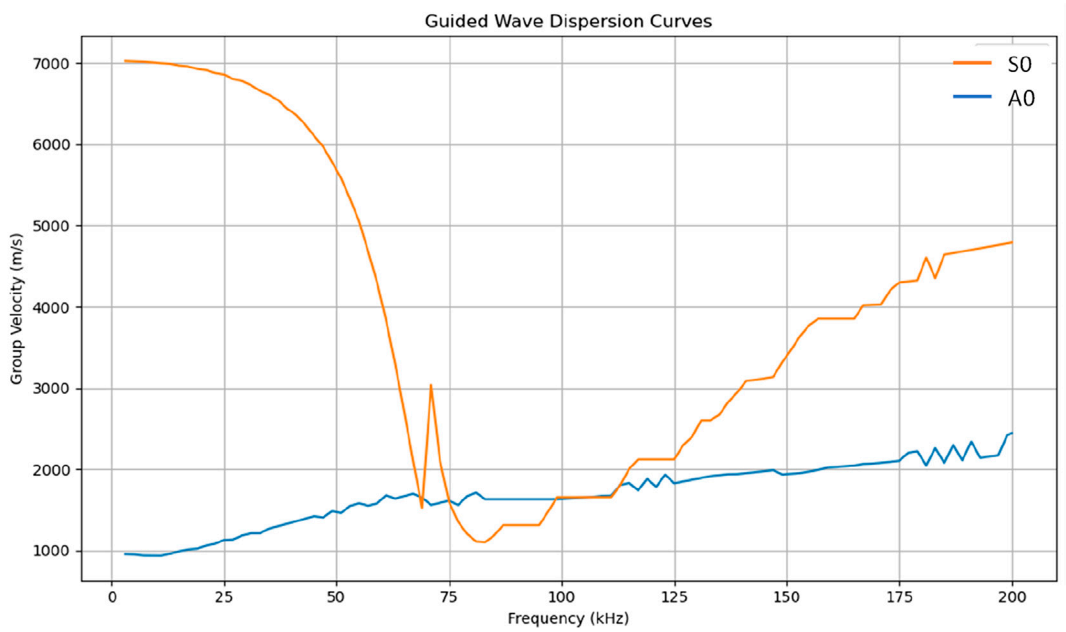

FIGURE 8
Group velocity dispersion curves of guided wave propagation in the GFRC.

5 Results and discussion

The experimental and numerical response of the healthy and damaged WTB models, along with the theoretically obtained dispersion curves, are explained in this section. The variations in amplitude and group velocity of the guided wave modes for each damage condition are also discussed in detail.

5.1 Dispersion of guided waves in WTB

The guided wave dispersion curves for the pristine WTB sample are obtained by using an established semi-analytical model explicitly described in Pol and Banerjee (2013). The global-matrix method-based theoretical model of guided wave propagation in the WTB is prepared in Fortran for 500 k iterations. The model uses the elastic material properties of the composite blade as per Table 1, 3 mm thickness, 0–200 kHz frequency range, and free-free boundary conditions. In the model, the dispersion condition for the propagating guided wave modes is given by Equation 23

$$V(\xi, \omega) = 0 \tag{23}$$

For the desired range of wave propagation frequency, 'ω', wavenumber 'ξ' components were calculated, and the corresponding frequency vs. group-velocity, 'V_g' dispersion curves are obtained for the real roots of 'ξ' from the equation given below

$$V_g = \frac{\delta\omega}{\delta\xi} \tag{24}$$

The dispersion curves are calculated as per Equation 24 and presented in Figure 8. The plot clearly shows the group velocities of the primary symmetric (S0) and anti-symmetric (A0) guided wave modes at the operating frequency of 150 kHz. The calculated dispersion values are used to identify the primary wave modes in the numerical and experimental signals in the time domain. The spikes observed in the dispersion curves result from numerical instabilities in the root-solving process and do not affect the identification of the guided wave modes.

5.2 Comparison between experimental and numerical responses for WTB models

The time-domain response (time in microseconds (μs) versus amplitude in millimetres (mm)) obtained at the sensing location using both experiments and FE analysis for the healthy WTB, WTB with edge erosion (25 mm long), WTB with longitudinal debond (35 mm × 6.5 mm), and WTB with transverse debond (45 mm × 6.5 mm), generated by a predefined actuation signal (150 kHz), is shown in Figure 9. The waveform plot from the FE simulation is presented in Figure 10. The raw voltage signals measured by the PZT sensors were converted to equivalent out-of-plane displacement (mm) through a calibration process. Representing the measurements as displacement facilitates interpretation of guided wave amplitudes and their variations due to damage (Giurgiutiu, 2014).

The obtained signal shows the presence of two primary Guided wave modes, identified as S0 and A0 modes, as observed from Figures 9a–d. The S0 mode is the symmetric mode, and the A0 mode is the anti-symmetric mode. This ordering and separation of modes agree well with the theoretical dispersion characteristic at the chosen excitation frequency (150 kHz). The experimental and numerical guided wave signals exhibit consistent waveform patterns and phase behaviour, with minor amplitude variations attributed to different

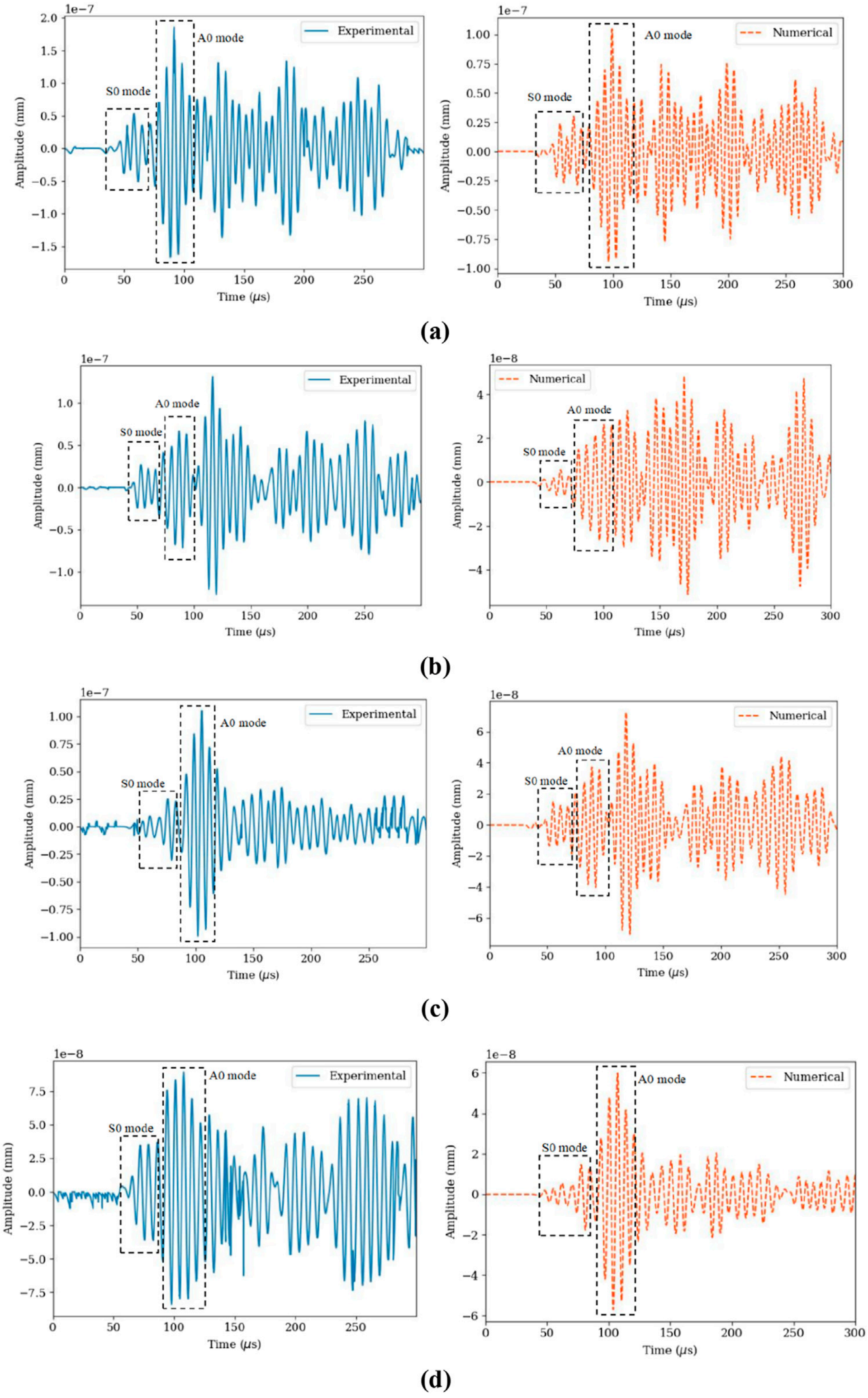

FIGURE 9
The time domain response obtained at the sensing location using experiment and FE analysis for **(a)** healthy WTB, **(b)** WTB with edge erosion (25 mm long), **(c)** WTB with longitudinal debond (35 mm × 6.5 mm) and **(d)** WTB with transverse debond (45 mm × 6.5 mm).

amplification ranges applied during acquisition. The Spearman correlation between the experimental and numerical signals for healthy WTB, WTB with edge erosion/corrosion, WTB with longitudinal debond and WTB with transverse debond is 92.8%, 93.41%, 95.26% and 92.60% respectively. These correlations indicate a high level of agreement between the experimental and numerical

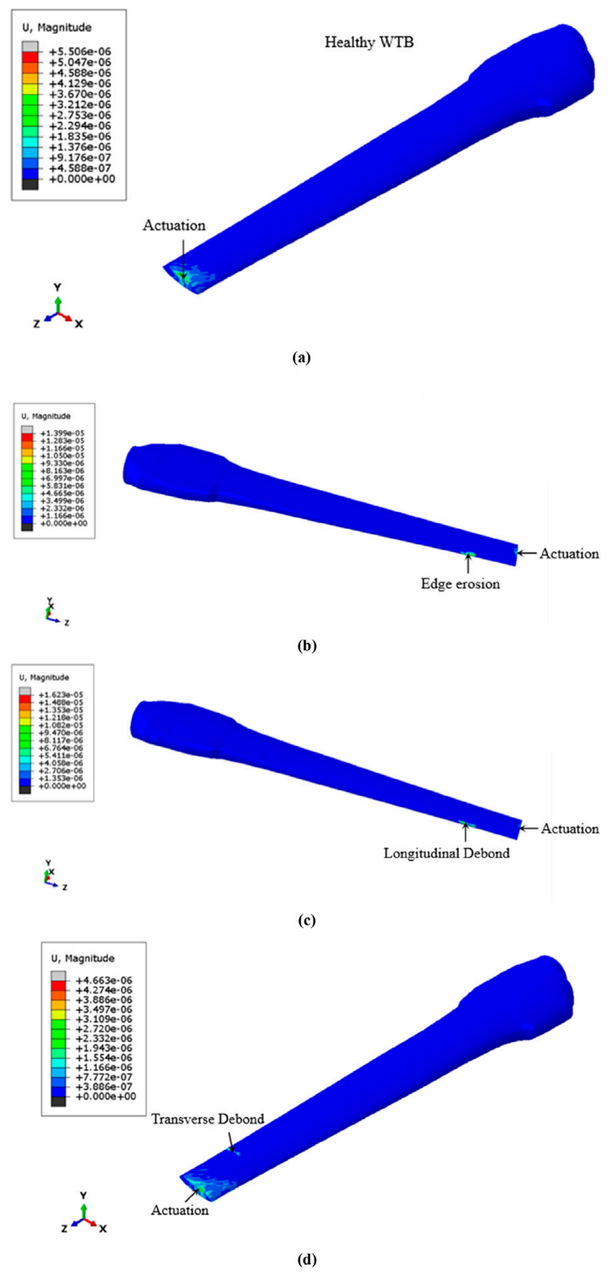

FIGURE 10
Waveform plots from FE simulation of the WTBs under **(a)** healthy **(b)** edge erosion/corrosion **(c)** longitudinal debond, and **(d)** transverse debond conditions.

signals for the healthy and damaged states of WTB. The different amplification ranges applied during acquisition contribute to the remaining 5–8% deviation. Further, the close agreement between experimental and numerical results confirmed that the influence of noise was negligible.

It is observed that due to the presence of damage, the amplitude of the output signals is reduced in each mode, i.e., S0 and A0 modes, as compared to the healthy condition for both experimental and FE analysis. The reason attributed to the reduction in amplitude is the wave attenuation, which occurs when the guided waves interact with damage. This is because the energy absorption increases due to the presence of damage in comparison to the healthy WTB model. Moreover, these structures are composed of complex layers of materials. This anisotropy due to different ply-orientations causes a directional dependency resulting in additional pulses, which can be observed from Figures 9a–d. At the excitation frequency of 150 kHz, the corresponding wavelengths for the A0 and S0 modes are 12.11 mm and 20.39 mm, respectively. This results in approximately 24 elements per wavelength for the A0 mode and 41 elements per wavelength for the S0 mode, ensuring sufficient spatial resolution for accurate propagation of guided waves. The mesh thus satisfies the commonly recommended criterion of more than 10 elements per wavelength for numerical stability and precision in wave propagation analysis (Landskron et al., 2025). The reduction in amplitudes with damaged WTB in comparison to the healthy WTB can also be observed from the waveform plots in Figures 10a–d.

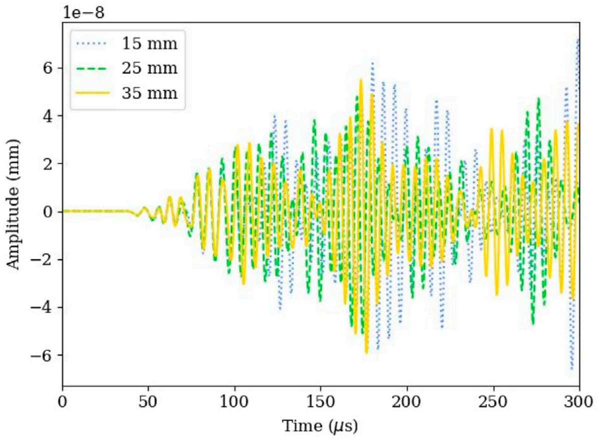

FIGURE 11
Variation of output response for different edge erosion/ corrosion size.

5.3 Parametric study of damage

The effect of the size of damage is important for the health monitoring of a WTB using guided waves. In order to understand this effect on the guided wave signal, a parametric study has been carried out in ABAQUS.

5.3.1 Edge erosion damage

Edge erosion/corrosion damage is induced for elements of size 15 mm × 5 mm, 25 mm × 5 mm and 35 mm × 5 mm. The elastic properties of these elements were modified based on their thickness, which was considered as 1×10^{-6} mm. The material properties corresponding to damage were taken from Table 2, and the elastic properties for the elements without damage were considered from Table 1.

The response is obtained at the sensing location for various damage sizes as mentioned above and compared with the healthy WTB model. The healthy case is treated as a no-damage condition with a zero length (0 mm) as a reference.

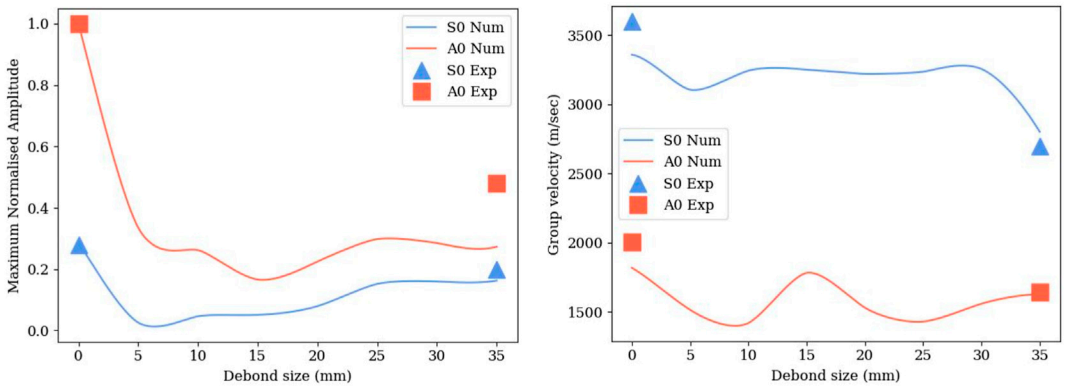

(a) **(b)**

FIGURE 12
Comparison of **(a)** maximum normalised amplitude, **(b)** group velocity with edge erosion/corrosion size for S0 and A0 modes.

The theoretical group velocities for the healthy and damaged WTB models using numerical analysis are compared with the experimental results. In the experiment and numerical analysis, signals are collected at a distance (Δx) of 150 mm from the actuation point. The time difference (Δt) between the peak of each envelope of a wave group for the actuation signal and receiver signal (signal obtained at the sensing point) is determined. This time shift is then determined for different modes, and the corresponding group velocity, V_g, is obtained employing a TOF analysis (Baid et al., 2015; Mustapha et al., 2011). V_g is determined as $\frac{\Delta x}{\Delta t}$.

The output responses for the numerical simulation for varying damage size are shown in Figure 11. The comparison of damage lengths (5 mm × 5 mm, 10 mm × 5 mm, 15 mm × 5 mm, 20 mm × 5 mm, 25 mm × 5 mm, 30 mm × 5 mm and 35 mm × 5 mm) and the corresponding maximum normalised amplitude and group velocity of S0 and A0 modes are shown in Figure 12.

It is observed from Figure 11 that edge erosion/corrosion reduces the local stiffness of the laminate and disrupts the wave propagation path. The normalized amplitude trends in Figure 12a further reinforce this observation. The A0 mode exhibits a rapid decrease in amplitude even for small erosion sizes, demonstrating strong sensitivity to edge erosion/corrosion. This is expected due to local loss of stiffness. However, the S0 mode shows a more gradual reduction in amplitude. In Figure 12b, the A0 mode exhibits variation in group velocity with increasing edge erosion/corrosion size due to its sensitivity to local bending stiffness reduction caused by material loss. Meanwhile, the S0 mode shows only minor variations in group velocity, indicating that small levels of erosion do not significantly alter in-plane stiffness. Although the relative changes in group velocity for S0 and A0 modes are comparable, the A0 mode remains the more useful damage indicator for early-stage debonding because it shows a larger amplitude drop at small debond sizes and more complex velocity variation around intermediate debond sizes.

Collectively, the amplitude and velocity results demonstrate that the A0 mode is substantially more sensitive to edge erosion and debond growth than the S0 mode. This sensitivity is advantageous for early-stage damage detection and localisation, while the S0 mode's stability can be beneficial for reliable signal transmission in structural health monitoring systems. The complementary behaviour of the two modes suggests that a multimodal Lamb-wave approach can provide enhanced robustness and improved diagnostic capability for detecting and characterising edge-related degradation in plate-like structures.

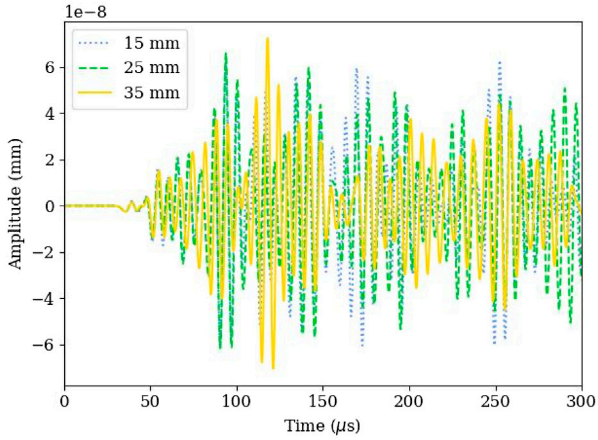

FIGURE 13
Comparison of output response for different longitudinal debond lengths.

The S0 and A0 modes are not pure modes due to the complex geometry of the WTB and the composite material construction. This mode impurity introduces minor uncertainty, especially at large defect sizes. The group velocity extraction experiences small shifts in arrival-time identification due to overlapping wave modes. However, the relative variation with defect size remains monotonic and physically consistent; the observed trends are reliable, even if the modes are not perfectly isolated.

5.3.2 Longitudinal debond

The WTB is partitioned in the longitudinal direction into small elements of dimensions 15, 25 and 35 mm. The material properties

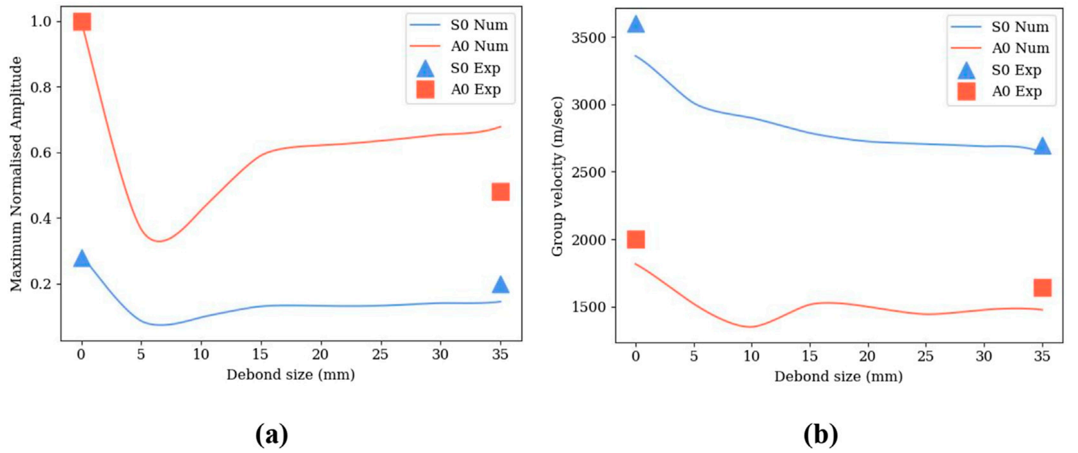

FIGURE 14
Comparison of **(a)** maximum normalised amplitude, **(b)** group velocity with debond size for S0 and A0 modes.

for these partitioned elements are detailed in Table 2, while the material properties for the remaining portion of the blade are given in Table 1. The elastic properties considered for the partitioned elements of size 15, 25 and 35 mm are described in Section 3.1, while the zero length (0 mm) is considered as a no damage case and is used as a healthy case. The numerical response with variation in the length of debond is shown in Figure 13.

The variation of maximum normalised amplitude and group velocity of S0 and A0 modes with debond size of 5 mm, 10 mm, 15 mm, 20 mm, 25 mm, 30 mm and 35 mm using experimental and numerical analysis is shown in Figure 14.

As the longitudinal debond length increases from 15 mm to 35 mm, the measured signals exhibit changes in amplitude of the S0 and A0 modes, as observed from Figure 13. This is due to the reduction in stiffness and transmission through the damaged areas. From Figure 14a, it can be observed that the S0 mode experiences a reduction in amplitude for small debond sizes, indicating that it is responsive to the initiation of longitudinal debond. The A0 mode shows an initial dip in amplitude followed by a gradual increase for larger debonds. This rise in amplitude for 25–35 mm debonds is characteristic of flexural waves interacting with extended delamination, where out-of-plane bending motion becomes amplified due to reduced through-thickness constraint. The group velocity decreases consistently with increasing debond length for the S0 mode, as observed from Figure 14b. This behaviour is due to the reduction in effective in-plane stiffness and increased scattering in the damaged region, which slows the extensional mode. The A0 mode, however, displays a non-monotonic trend: its velocity initially decreases, reaching a minimum at intermediate debond sizes, and then increases slightly for larger debonds. This behaviour is governed by stiffness loss and dispersion-induced energy redistribution.

5.3.3 Transverse debond

The WTBs are partitioned in the transverse direction. The size of the partition elements is 15, 25 and 35 mm. The material properties and elastic properties considered for these elements are given in Table 2 and mentioned in Section 3.1. The elastic properties for the undamaged portion of the blade are taken from the values given in Table 1. The comparison of the response with the debond size is shown in Figure 15. The experimental and numerical variation of maximum normalised amplitude and group velocity of S0 and A0 modes with debond sizes of 5 mm–35 mm, with an increment of 5 mm, is shown in Figure 16.

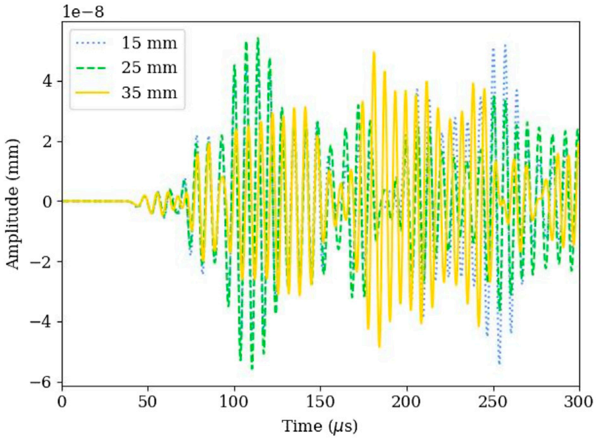

FIGURE 15
Variation in output response for different transverse debond sizes.

The contrasting amplitude trends observed for the S0 and A0 modes arise from their different deformation mechanisms, as observed from Figure 15. The S0 mode is dominated by in-plane extensional motion and relies on the through-thickness and inter-laminar stiffness of the laminate. As the transverse debond grows, this stiffness is progressively reduced, causing scattering and reflection of the S0 wave and consequently leading to a monotonic decrease in its measured amplitude. In contrast, the A0 mode is flexural in nature and is primarily governed by bending stiffness rather than in-plane rigidity. This reduction in bending resistance amplifies the flexural motion, resulting in an increase in A0 amplitude for larger debond sizes. Therefore, while both modes

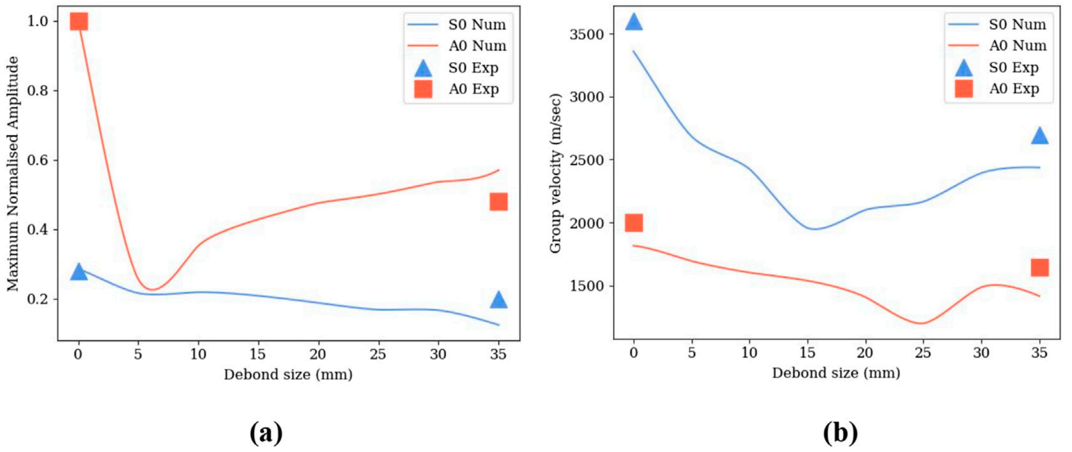

FIGURE 16
Variation of **(a)** maximum normalised amplitude, **(b)** group velocity for S0 and A0 modes with debond size.

are affected by the loss of stiffness, S0 amplitude diminishes due to energy loss through scattering, whereas A0 amplitude grows because the debond amplifies bending-dominated wave components. This variation can be observed in experimental and numerical results, as seen from Figure 16a for both S0 and A0 modes. The group velocity for the S0 mode decreases with debond length and then increases, due to the reduction in effective stiffness as the wave continuously encounters a larger damaged region, as observed from Figure 16b. Although this debond reduces local stiffness, the measured group velocity of the S0 mode increases because the defect filters out slower dispersive components. Additionally, scattering and redirection at the debond cause earlier-arriving S0 components to dominate the received signal, resulting in an increase in wave speed in the damaged WTB. The A0 mode displays a non-monotonic trend as observed from Figure 16b, where the velocity first decreases to a minimum at intermediate debond sizes (upto 20 mm), before increasing slightly at larger debond sizes. This behaviour arises because of the initial stiffness reduction and mode interaction at small or intermediate sizes.

It should be noted that because of the limited number of available specimens and certain experimental restrictions, only two representative defect sizes were examined experimentally in this study. To complement these results, additional numerical simulations were performed for intermediate defect sizes, confirming a consistent relationship between amplitude reduction and defect dimension.

5.3.4 UQ for extended prediction

UQ was carried out on the outputs of the Random Forest model using the numerical simulation dataset, which encompassed different defect sizes (0–40 mm) and types, including edge erosion/corrosion, longitudinal debonding, and transverse debonding.

The 95% confidence intervals were calculated by taking the standard deviation of predictions across all decision trees in the ensemble, reflecting variability in the model's responses. The sample size corresponds to the total number of prediction cases derived from these simulated damage scenarios used during model training and testing. Experimental results were utilized solely for model validation. The sample size corresponds to the total number of prediction cases generated from multiple guided-wave measurements covering all damage types and sizes. Each damage class includes a sufficient number of samples to ensure statistical robustness, typically ranging from 10 to 100 samples per class.

As described in Section 4, this subsection focuses on UQ of the Random Forest model's predictions for changes in A_0 and S_0 mode group velocities (V_g) caused by edge erosion/corrosion, longitudinal debond, and transverse debond over damage sizes ranging from 0 to 40 mm. The model was developed using a relatively small, targeted dataset corresponding to eight distinct damage sizes across various damage types. This dataset, compiled from both experimental measurements and validated numerical simulations, proved sufficient given the specific nature of the prediction task. To ensure reliable learning, approximately 70% of the data was used for training and 30% for testing, maintaining balanced representation of all damage sizes. To prevent overfitting and enhance model generalisation, 5-fold cross-validation was applied during the training phase. This approach allowed the Random Forest model to be validated on multiple data partitions, thereby reducing bias and variance and ensuring robust performance across unseen data.

Figure 17 illustrates the predicted changes in group velocity with uncertainty bands representing 95% confidence intervals. These bands are calculated based on the standard deviation of predictions across individual trees in the Random Forest model, offering a measure of prediction confidence. Narrower uncertainty bands indicate higher confidence in the model's predictions, while wider bands reflect greater variability and uncertainty. In Figure 17, L-Debond represents Longitudinal Debond and T-Debond represents Transverse Debond.

Similarly, Figure 18 illustrates the relative variation in A0 and S0 mode amplitudes with respect to the different damage types (Edge Erosion/corrosion, Longitudinal Debond, and Transverse Debond) and their sizes, with uncertainty bands representing the 95% confidence intervals around the predicted values. In Figure 18,

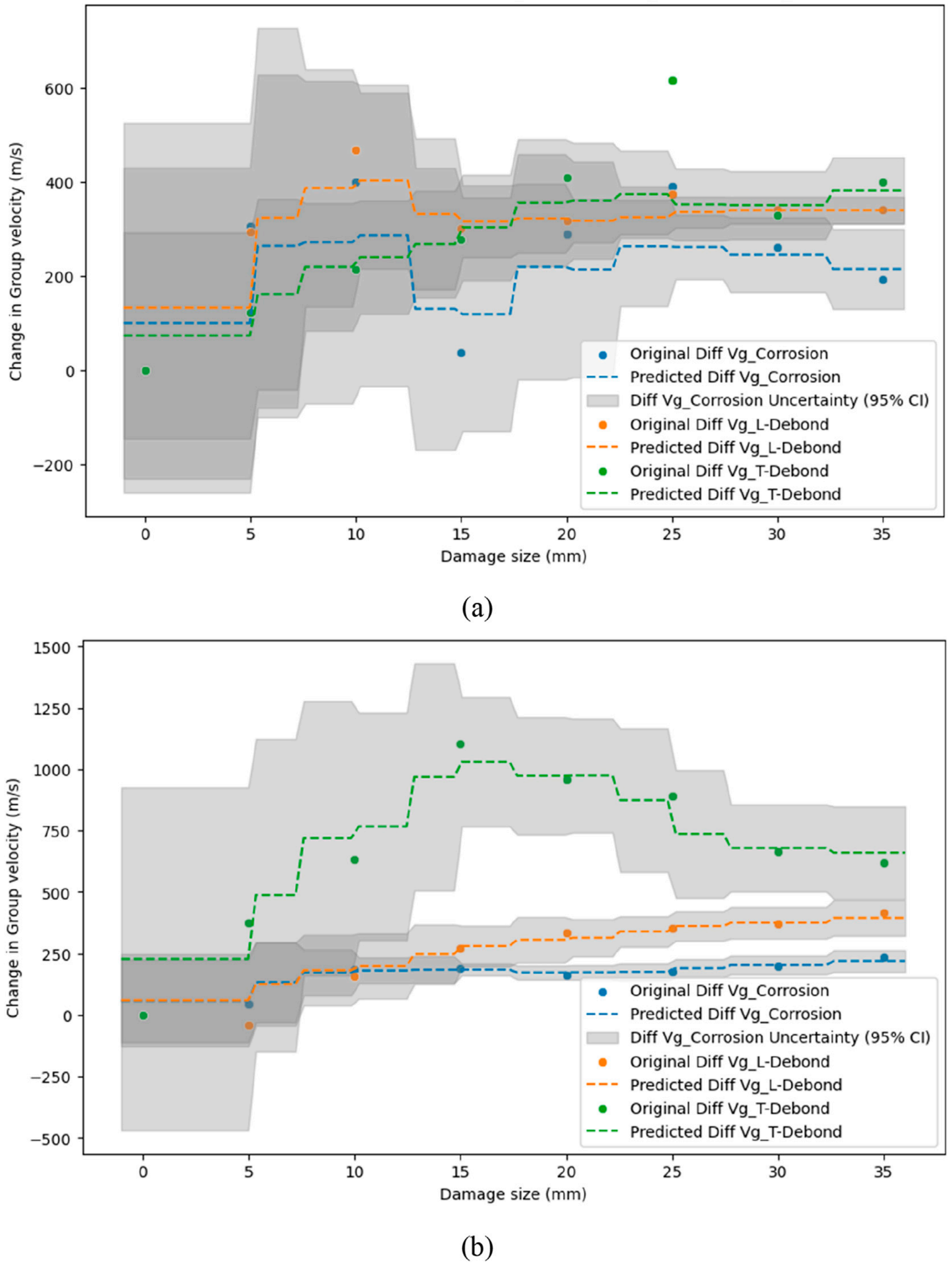

(a)

(b)

FIGURE 17
Damage size vs. change in **(a)** A0 and **(b)** S0 mode group velocities due to Edge Erosion/corrosion, L-Debond, and T-Debond, with uncertainty bands.

L-Debond and T-Debond represents Longitudinal Debond and Transverse Debond respectively.

Figures 17, 18 present the effect of different defect types and sizes on guided wave features, along with associated prediction uncertainties. The results show that the S_0 mode exhibits higher sensitivity to variations in defect size compared to the A_0 mode, indicating its greater suitability for detecting and characterizing damage in composite wind turbine blades. The confidence intervals reflect the variability in model predictions, where narrower intervals suggest higher confidence and stability of the results. Here, “higher sensitivity” refers to the stronger and more consistent changes observed in the S0 mode’s group velocity and amplitude as defect size increases, compared to the A0 mode. This is evident from the steeper trends and larger

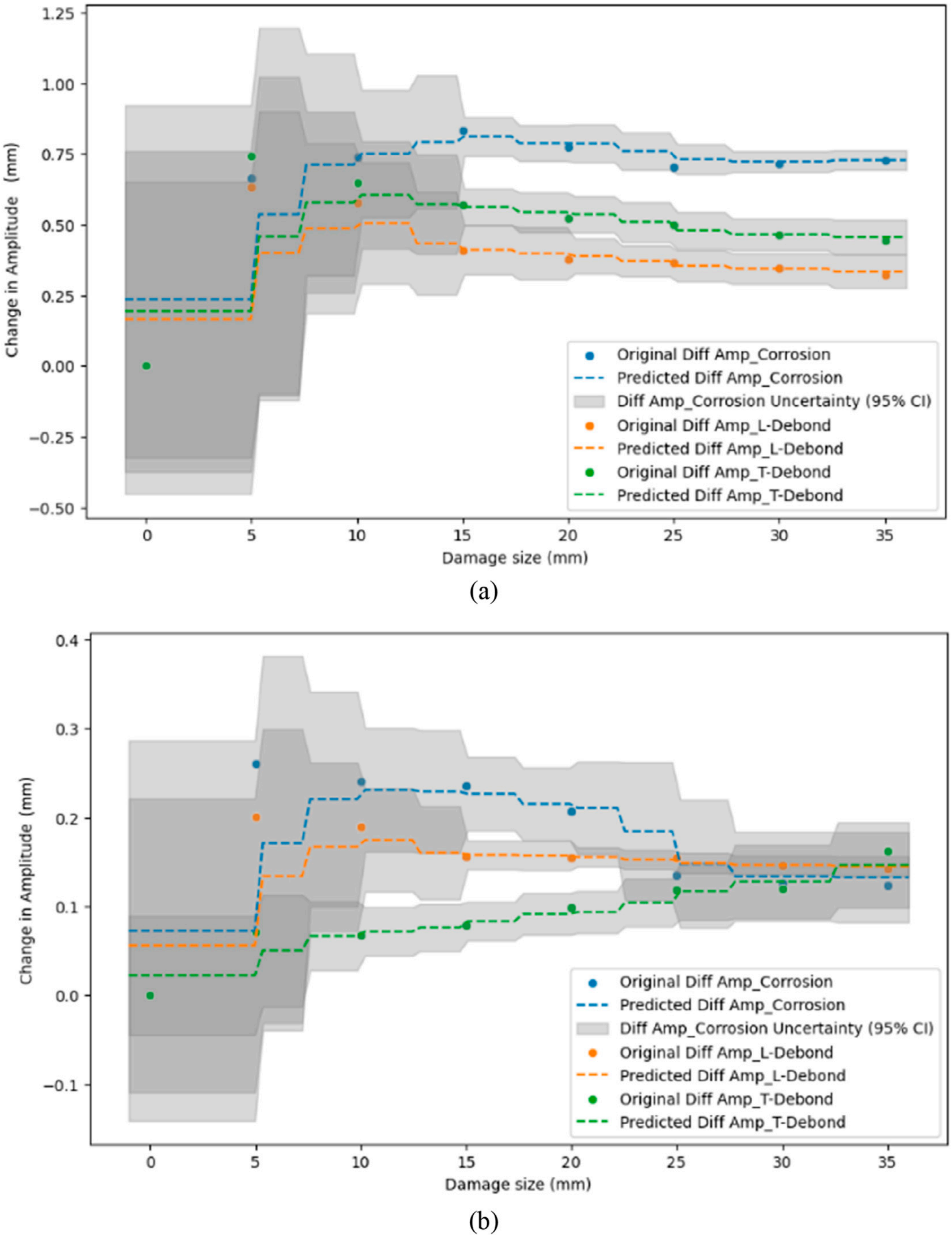
(a)

(b)

FIGURE 18
Damage size vs. change in **(a)** A0 and **(b)** S0 mode amplitudes due to Edge Erosion, L-Debond, and T-Debond, with uncertainty bands representing the 95% confidence intervals.

variation magnitudes in Figures 17, 18, along with narrower uncertainty bands for the S0 mode, indicating more reliable and robust damage detection. These findings provide practical guidance for selecting appropriate excitation frequencies (100–200 kHz) and wave modes for field-scale guided-wave inspection of GFRC blades, enabling more accurate and reliable damage detection. The 95% confidence intervals were chosen due to their ease of computation and straightforward interpretability. Uncertainty is effectively captured by utilizing the variability in predictions from individual trees within the Random Forest ensemble, without significantly increasing computational demands. Although more advanced methods, such as Bayesian approaches, can offer deeper probabilistic insights, they often require increased model complexity and computational resources. Given the practical focus of this study, use of this confidence intervals was considered appropriate. More sophisticated UQ methods may be explored in future work to enhance prediction robustness.

6 Conclusion

This study investigated guided wave propagation and its interaction with various types of damage for structural health monitoring of composite wind turbine blades. Experimental testing, numerical simulations, and UQ were combined to evaluate the sensitivity of guided wave parameters to different defect sizes and types. The key findings include:

- Guided-wave responses in composite blades showed multimodal characteristics, with significant amplitude reductions observed in damaged specimens due to energy scattering and absorption.
- Damage types influenced the S0 and A0 modes differently: A0 mode is sensitive to edge erosion/corrosion, while S0 mode is sensitive to longitudinal debond; both S0 and A0 modes are sensitive to transverse debond.
- Damage types influenced wave propagation velocities differently: the group velocity for the A0 mode changes with increasing edge erosion or corrosion due to its sensitivity to reduced bending stiffness, while the S0 mode shows only slight velocity changes, indicating minimal impact on in-plane stiffness; increasing longitudinal debond length consistently reduces the S0 mode group velocity due to diminished in-plane stiffness, while the A0 mode exhibits a non-monotonic response, with its velocity decreasing at intermediate debond sizes; the S0 mode shows an initial decrease followed by an increase in group velocity with increase in transverse debond length, due to reduced stiffness, while the A0 mode exhibits a non-monotonic trend, with its velocity decreasing to a minimum at intermediate debond sizes before slightly rising at larger ones, due to the combined effects of stiffness loss and mode interaction.
- UQ applied to Random Forest model predictions, expressed via 95% confidence intervals, indicated varying confidence levels, enhancing the robustness of damage assessment.
- The combined use of simulation and experimental data validates the framework's capability to correlate guided-wave features with damage progression effectively.

These results provide a practical basis for selecting optimal guided-wave modes and excitation frequencies (100–200 kHz) for field inspections of composite blades.

The use of low-frequency guided waves and edge computing-compatible algorithms reduces power consumption and hardware costs compared to more complex sensing techniques. Future work will focus on comprehensive economic and energy assessments to support practical deployment at scale.

The proposed framework lays the groundwork for advanced, intelligent structural health monitoring systems for composite wind turbine blades, with ongoing efforts aimed at autonomous, multi-level damage detection under realistic operational conditions.

Data availability statement

The raw data supporting the conclusions of this article will be made available by the authors, without undue reservation.

Author contributions

AP: Validation, Writing – review and editing, Formal analysis, Software, Data curation, Writing – original draft, Resources, Investigation, Methodology, Conceptualization, Visualization. SS: Investigation, Writing – review and editing, Methodology, Supervision, Formal Analysis, Data curation, Writing – original draft, Software, Funding acquisition, Validation, Conceptualization, Resources, Visualization, Project administration.

Funding

The author(s) declared that financial support was received for this work and/or its publication. SS wishes to acknowledge the support from the University of Huddersfield's URF Grant: QR24E025.

Conflict of interest

The author(s) declared that this work was conducted in the absence of any commercial or financial relationships that could be construed as a potential conflict of interest.

Generative AI statement

The author(s) declared that generative AI was not used in the creation of this manuscript.

Any alternative text (alt text) provided alongside figures in this article has been generated by Frontiers with the support of artificial intelligence and reasonable efforts have been made to ensure accuracy, including review by the authors wherever possible. If you identify any issues, please contact us.

Publisher's note

References

ABAQUS, A. (2008). *Getting started with ABAQUS: interactive edition*. Providence, RI: Dassault Systemes Simulia Corp.Tech. Available online at: https://scholar.google.com/scholar?hl=en&as_sdt=0%2C5&q=ABAQUS%2C+A.+%282008%29.+Getting+started+with+ABAQUS%3A+interactive+edition.+Providence%2C+RI%3A+Dassault+Systemes+Simulia+Corp.Tech.+Rep.&btnG=.

ABAQUS (2017). *Delamination analysis of laminated composites.* mit.edu.

Akhtar, N., Geyer, B., and Schrum, C. (2024). Larger wind turbines as a solution to reduce environmental impacts. *Sci. Rep.* 14 (1), 6608. doi:10.1038/s41598-024-56731-w

Algolfat, A., Wang, W., and Albarbar, A. (2023). The sensitivity of 5MW wind turbine blade sections to the existence of damage. *Energies* 16 (3), 1367. doi:10.3390/en16031367

Baid, H., Schaal, C., Samajder, H., and Mal, A. (2015). Dispersion of lamb waves in a honeycomb composite sandwich panel. *Ultrasonics* 56, 409–416. doi:10.1016/j.ultras.2014.09.007

Barr, S. M., and Jaworski, J. W. (2019). Optimization of tow-steered composite wind turbine blades for static aeroelastic performance. *Renew. Energy* 139, 859–872. doi:10.1016/j.renene.2019.02.125

Bejger, A., Drzewieniecki, J. B., Bartoszko, P., and Frank, E. (2023). The use of coherence functions of acoustic emission signals as a method for diagnosing wind turbine blades. *Energies* 16 (22), 7474. doi:10.3390/en16227474

Boudounit, H., Tarfaoui, M., Saifaoui, D., and Nachtane, M. (2020). Structural analysis of offshore wind turbine blades using finite element method. *Wind Eng.* 44 (2), 168–180. doi:10.1177/0309524X19849830

Camanho, P. P. (2002). "Failure criteria for fibre-reinforced polymer composites," in *Secção de Mecânica Aplicada, Departamento de Engenharia Mecânica e Gestão Industrial.* Faculdade de Engenharia da Universidade do Porto.

Chai, Y., Wu, Q., Yan, J., Liu, Q., and Qing, X. (2025). Failure monitoring and localization of wind turbine blades using ultrasonic guided waves and multi-index fusion imaging. *Eng. Fail. Anal.* 170, 109326. doi:10.1016/j.engfailanal.2025.109326

Claytor, T. N., Ammerman, C. N., Park, G. H., Farinholt, K. M., Farrar, C. R., and Atterbury, M. K. (2010). *Structural damage identification in wind turbine blades using piezoelectric active sensing with ultrasonic validation (No. LA-UR-10-00416; LA-UR-10-416).* Los Alamos, NM: Los Alamos National Laboratory.

Dadashbaki, F., Sikdar, S., Walton, K., and Mishra, R. (2025). Nondestructive structural health monitoring of composite wind turbine blades using acoustic emission. *Int. J. Syst. Assur. Eng. Manag.* 1–6. doi:10.1007/s13198-025-03007-9

Dimitrova, M., Aminzadeh, A., Meiabadi, M. S., Sattarpanah Karganroudi, S., Taheri, H., and Ibrahim, H. (2022). A survey on non-destructive smart inspection of wind turbine blades based on industry 4.0 strategy. *Appl. Mech.* 3 (4), 1299–1326. doi:10.3390/applmech3040075

Gaidai, O., Yakimov, V., Wang, F., Zhang, F., and Balakrishna, R. (2023). Floating wind turbines structural details fatigue life assessment. *Sci. Rep.* 13 (1), 16312. doi:10.1038/s41598-023-43554-4

Giurgiutiu, V. (2005). Tuned lamb wave excitation and detection with piezoelectric wafer active sensors for structural health monitoring. *J. Intelligent Material Systems Structures* 16 (4), 291–305. doi:10.1177/1045389X05050106

Giurgiutiu, V. (2014). *Structural health monitoring with piezoelectric wafer active sensors*. Academic Press.

Giurgiutiu, V., Zagrai, A., and Jing Bao, J. (2002). Piezoelectric wafer embedded active sensors for aging aircraft structural health monitoring. *Struct. Health Monit.* 1 (1), 41–61. doi:10.1177/147592170200100104

Gómez Muñoz, C. Q., García Márquez, F. P., Hernández Crespo, B., and Makaya, K. (2019). Structural health monitoring for delamination detection and location in wind turbine blades employing guided waves. *Wind Energy* 22 (5), 698–711. doi:10.1002/we.2316

Grindheim, O. M., Xing, Y., and Impelluso, T. (2023). Dynamic analysis and validation of a multi-body floating wind turbine using the moving frame method. *Front. Mech. Eng.* 9, 1156721. doi:10.3389/fmech.2023.1156721

Habibi, H., Cheng, L., Zheng, H., Kappatos, V., Selcuk, C., and Gan, T. H. (2015). A dual de-icing system for wind turbine blades combining high-power ultrasonic guided waves and low-frequency forced vibrations. *Renew. Energy* 83, 859–870. doi:10.1016/j.renene.2015.05.025

Hashin, Z. (1980). Failure criteria for unidirectional fiber composites. *J. Appl. Mech.* 47 (2), 329–334. doi:10.1115/1.3153664

Hashin, Z., and Rotem, A. (1973). A fatigue failure criterion for fiber reinforced materials. *J. Composite Materials* 7 (4), 448–464. doi:10.1177/002199837300700404

Hay, T. R., Wei, L., Rose, J. L., and Hayashi, T. (2003). Rapid inspection of composite skin-honeycomb core structures with ultrasonic guided waves. *J. Compos. Mater.* 37 (10), 929–939. doi:10.1177/0021998303037010005

Humer, C., Höll, S., Kralovec, C., and Schagerl, M. (2022). Damage identification using wave damage interaction coefficients predicted by deep neural networks. *Ultrasonics* 124, 106743. doi:10.1016/j.ultras.2022.106743

Joosse, P. A., Blanch, M. J., Dutton, A. G., Kouroussis, D. A., Philippidis, T. P., and Vionis, P. S. (2002). Acoustic emission monitoring of small wind turbine blades. *J. Sol. Energy Eng.* 124 (4), 446–454. doi:10.1115/1.1509769

Junqueira, B. F., Leiderman, R., and Castello, D. A. (2024). Damage recovery in composite laminates through deep learning from acoustic scattering of guided waves. *Ultrasonics* 139, 107293. doi:10.1016/j.ultras.2024.107293

Kalgutkar, A. P., and Banerjee, S. (2024). Interaction of ultrasonic guided waves with interfacial debonding in a stiffened composite plate under variable temperature and operational conditions. *Ultrasonics* 142, 107378. doi:10.1016/j.ultras.2024.107378

Landskron, J., Backer, A., Wolf, C. R., Fischerauer, G., and Drese, K. S. (2025). FEM-based modeling of guided acoustic waves on free and fluid-loaded plates. *Appl. Sci.* 15 (16), 9116. doi:10.3390/app15169116

Lanza Discalea, F., Matt, H., Bartoli, I., Coccia, S., Park, G., and Farrar, C. (2007). Health monitoring of UAV wing skin-to-spar joints using guided waves and macro fiber composite transducers. *J. Intelligent Material Systems Structures* 18 (4), 373–388. doi:10.1177/1045389X06066528

Lapczyk, I., and Hurtado, J. A. (2007). Progressive damage modeling in fiber-reinforced materials. *Compos. Part A Appl. Science Manufacturing* 38 (11), 2333–2341. doi:10.1016/j.compositesa.2007.01.017

Li, X., Yang, Z., Zhang, H., Du, Z., and Chen, X. (2014). Crack growth sparse pursuit for wind turbine blade. *Smart Materials Structures* 24 (1), 015002. doi:10.1088/0964-1726/24/1/015002

Lowe, M. J. S., Challis, R. E., and Chan, C. W. (2000). The transmission of lamb waves across adhesively bonded lap joints. *J. Acoust. Soc. Am.* 107 (3), 1333–1345. doi:10.1016/j.phpro.2015.08.012

Maas, O. (2023). Large-eddy simulation of a 15 GW wind farm: flow effects, energy budgets and comparison with wake models. *Front. Mech. Eng.* 9, 1108180. doi:10.3389/fmech.2023.1108180

Márquez, F. P. G., Tobias, A. M., Pérez, J. M. P., and Papaelias, M. (2012). Condition monitoring of wind turbines: techniques and methods. *Renew. Energy* 46, 169–178. doi:10.1016/j.renene.2012.03.003

Matzenmiller, A. L. J. T. R., Lubliner, J., and Taylor, R. L. (1995). A constitutive model for anisotropic damage in fiber-composites. *Mech. Materials* 20 (2), 125–152. doi:10.1016/0167-6636(94)00053-0

Mendikute, J., Carmona, I., Aizpurua, I., Bediaga, I., Castro, I., Galdos, L., et al. (2025). Defect detection in wind turbine blades applying convolutional neural networks to ultrasonic testing. *NDT and E Int.* 154, 103359. doi:10.1016/j.ndteint.2025.103359

Mustapha, S., Ye, L., Wang, D., and Lu, Y. (2011). Assessment of debonding in sandwich CF/EP composite beams using A0 lamb wave at low frequency. *Compos. Structures* 93 (2), 483–491. doi:10.1016/j.compstruct.2010.08.032

Nam, M., Chi, S., and Lim, S. (2018). Application of phased array ultrasonic testing to detect delamination for wind turbine blade. *J. Wind Energy* 9 (3), 33–42. doi:10.33519/kwea.2018.9.3.005

Oliveira, M. A., Simas Filho, E. F., Albuquerque, M. C., Santos, Y. T., Da Silva, I. C., and Farias, C. T. (2020). Ultrasound-based identification of damage in wind turbine blades using novelty detection. *Ultrasonics* 108, 106166. doi:10.1016/j.ultras.2020.106166

Ou, Y., Tatsis, K. E., Dertimanis, V. K., Spiridonakos, M. D., and Chatzi, E. N. (2021). Vibration-based monitoring of a small-scale wind turbine blade under varying climate conditions. Part I: an experimental benchmark. *Struct. Control Health Monit.* 28 (6), e2660. doi:10.1002/stc.2660

Pol, C. B., and Banerjee, S. (2013). Modeling and analysis of propagating guided wave modes in a laminated composite plate subject to transient surface excitations. *Wave Motion* 50 (5), 964–978. doi:10.1016/j.wavemoti.2013.04.003

Raju, S. K., Natesan, S., Alharbi, A. H., Kannan, S., Khafaga, D. S., Periyasamy, M., et al. (2024). AHP VIKOR framework for selecting wind turbine materials with a focus on corrosion and efficiency. *Sci. Rep.* 14 (1), 24071. doi:10.1038/s41598-024-72761-w

Schubel, P. J., Crossley, R. J., Boateng, E. K. G., and Hutchinson, J. R. (2013). Review of structural health and cure monitoring techniques for large wind turbine blades. *Renew. Energy* 51, 113–123. doi:10.1016/j.renene.2012.08.072

Schulz, M. J., and Sundaresan, M. J. (2006). *Smart sensor system for structural condition monitoring of wind turbines.* Denver, Colorado: National Renewable Energy Laboratory.

Shoja, S., Berbyuk, V., and Boström, A. (2018). Guided wave–based approach for ice detection on wind turbine blades. *Wind Eng.* 42 (5), 483–495. doi:10.1177/0309524x18754767

Sikdar, S., and Banerjee, S. (2016). Guided wave propagation in a honeycomb composite sandwich structure in presence of a high density core. *Ultrasonics* 71, 86–97. doi:10.1016/j.ultras.2016.05.025

Sikdar, S., Gullapalli, A., and Kundu, A. (2024). A hierarchical multistage holistic model for acoustic emission source monitoring in composites. *Smart Mater. Struct.* 33 (11), 115022. doi:10.1088/1361-665X/ad8409

Sinner, M., Petrović, V., Stockhouse, D., Langidis, A., Pusch, M., Kühn, M., et al. (2023). Insensitivity to propagation timing in a preview-enabled wind turbine control experiment. *Front. Mech. Eng.* 9, 1145305. doi:10.3389/fmech.2023.1145305

Skaga, S. K. (2017). "Feasibility study of unmanned aerial vehicles (UAV) application for ultrasonic non-destructive testing (NDT) of wind turbine rotor blades. Preliminary experiments of handheld and UAV ultrasonic testing on glass fibre laminate," in *Master's thesis, UiT the arctic university of Norway, tromsø, Norway*.

Su, Z., Ye, L., and Bu, X. (2002). A damage identification technique for CF/EP composite laminates using distributed piezoelectric transducers. *Compos. Structures* 57 (1-4), 465–471. doi:10.1016/S0263-8223(02)00115-0

Taylor, S. G., Farinholt, K. M., Jeong, H., Jang, J., Park, G. H., Todd, M. D., et al. (2012). *Wind turbine blade fatigue tests: lessons learned and application to SHM system development (No. LA-UR-12-22587)*. Los Alamos, NM: Los Alamos National Laboratory.

Verijenko, B., and Verijenko, V. (2005). A new structural health monitoring system for composite laminates. *Compos. Structures* 71 (3-4), 315–319. doi:10.1016/j.compstruct.2005.09.024

Warren, K. C., Lopez-Anido, R. A., Vel, S. S., and Bayraktar, H. H. (2016). Progressive failure analysis of three-dimensional woven carbon composites in single-bolt, double-shear bearing. *Compos. Part B Eng.* 84, 266–276. doi:10.1016/j.compositesb.2015.08.082

Xue, S., Zhou, W., Beck, J. L., Huang, Y., and Li, H. (2023). Damage localization and robust diagnostics in guided-wave testing using multitask complex hierarchical sparse Bayesian learning. *Mech. Syst. Signal Process.* 197, 110365. doi:10.1016/j.ymssp.2023.110365

Yan, Y. J., Cheng, L., Wu, Z. Y., and Yam, L. H. (2007). Development in vibration-based structural damage detection technique. *Mech. Systems Signal Processing* 21 (5), 2198–2211. doi:10.1016/j.ymssp.2006.10.002

Yang, K., Rongong, J. A., and Worden, K. (2018). Damage detection in a laboratory wind turbine blade using techniques of ultrasonic NDT and SHM. *Strain* 54 (6), e12290. doi:10.1111/str.12290

Zhang, H., and Jackman, J. (2014). Feasibility of automatic detection of surface cracks in wind turbine blades. *Wind Eng.* 38 (6), 575–586. doi:10.1260/0309-524x.38.6.575

Zhang, Y., Avallone, F., and Watson, S. (2022). Wind turbine blade trailing edge crack detection based on airfoil aerodynamic noise: an experimental study. *Appl. Acoust.* 191, 108668. doi:10.1016/j.apacoust.2022.108668

Zhao, H., Chen, G., Hong, H., and Zhu, X. (2021). Remote structural health monitoring for industrial wind turbines using short-range Doppler radar. *IEEE Trans. Instrum. Measurement* 70, 1–9. doi:10.1109/tim.2021.3053959

Zhu, X., Guo, Z., Zhou, Q., Zhu, C., Liu, T., and Wang, B. (2025). Damage identification of wind turbine blades based on deep learning and ultrasonic testing. *Nondestruct. Test. Eval.* 40 (2), 508–533. doi:10.1080/10589759.2024.2324373